Available online at www.sciencedirect.com

ScienceDirect

journal homepage: www.elsevier.com/locate/he

Effects of reactants/coolant non-uniform inflow on the cold start performance of PEMFC stack

Lin Wei [a,1], *Ahmed Mohmed Dafalla* [a,b,1], *Fangming Jiang* [a,*]

[a] *Laboratory of Advanced Energy Systems, CAS Key Laboratory of Renewable Energy, Guangdong Key Laboratory of New and Renewable Energy Research and Development, Guangzhou Institute of Energy Conversion, Chinese Academy of Sciences (CAS), China*

[b] *University of Chinese Academy of Sciences, China*

HIGHLIGHTS

- A 3D model for proton exchange membrane fuel cell cold start is presented.
- The model is used to study the non-uniform inflow effects of reactants/coolant.
- Obvious non-uniform inflow effects on ice formation and current density are seen.
- Parametric study about membrane hydration and stoichiometry is also carried out.

ARTICLE INFO

Article history:
Received 29 December 2019
Received in revised form
13 February 2020
Accepted 5 March 2020
Available online 27 March 2020

Keywords:
Proton exchange membrane fuel cell
Cold start
Coolant
Numerical model

ABSTRACT

The failure at equally distributing reactants among different channels within the stack leads to uneven reaction and gas concentration distribution in the catalyst layers, which consequently impacts the performance and durability of proton exchange membrane fuel cell stacks (PEMFCs). A three-dimensional, transient, non-isothermal cold start model for PEMFCs with parallel flow-field configuration and coolant circulation is developed in this work to investigate the effects of non-uniform distribution of reactants/coolant inflow rates on the cold start process. The results show that the effect of non-uniform inflow on ice formation amount is obvious and that on the distribution uniformity of current density is apparent over the cold start survival time. Additionally, the simulation predictions show that the non-uniform initial membrane water content distribution due to the purge procedure can significantly increase the rate of ice growth and deteriorate the uniformity of current density distribution in the membrane. It is found that high stoichiometry operating condition is favorable to cold startup, but may result in drying in the membrane at regions close to the channel inlet side. As non-uniform inflow rates issue is inevitable in actual PEMFC stack operation conditions, our results demonstrate that the initial membrane water content and cathode stoichiometry ratio need to be identified to moderate the effects of reactants/coolant inflow maldistribution and to maintain a stable cold start performance for the PEMFC stack.

* *Corresponding author*. Laboratory of Advanced Energy Systems, Guangzhou Institute of Energy Conversion, Chinese Academy of Sciences (CAS), 2 Nengyuan Rd, Wushan, Tianhe District, Guangzhou 510640, China.
E-mail address: fm_jiang2000@yahoo.com (F. Jiang).

[1] Co-first authors, both authors have equal contribution to this work.

https://doi.org/10.1016/j.ijhydene.2020.03.031
0360-3199/

Introduction

Proton exchange membrane fuel cell (PEMFC) is considered as one of the promising clean and suitable power sources for automotive applications [1,2], and also an attractive solution for the recent environmental pollution [3], owing to its high current density, low operating temperature, high efficiency and zero emission. However, the ability of PEMFCs to reach a temperature above the freezing point when it starts up from subzero temperature is significant for its commercialization [4]. As a result of both the electro-osmotic drag (EOD) effect and the oxygen reduction reaction (ORR) at the cathode side of PEMFC, the water accumulates at the cathode side. At sub-freezing temperatures, when the accumulated water exceeds the maximum water saturation, the water turns to ice. The continuous formation of ice in the catalyst layer (CL) can potentially block the reactants transport or may cover the area where the electrochemical reactions occur. The blockage and accumulation of ice in the cathode CL is a significant issue since it causes the cell voltage to drop or even shut-down [5,6]. Consequently, in order to achieve a successful self-startup from subzero temperature without external heating it is essential to promote the cell temperature above the freezing point (0 °C) before the CL is entirely filled up by ice, which can only be determined upon managing the balance between ice formation and heat generation [7–9]. A number of numerical and experimental studies have been carried out to elucidate the cold start behavior [6,10–16], and self-startup strategies for cold start have been proposed [9,17,18]. Accordingly, several models have been developed considering single cell [19–22] and stack configuration [23–26] to get a better understanding of the cold start behaviors.

The reactants distribution in PEMFC channels is crucial for fuel cells performance and efficiency, because it contributes to the water and heat management; the reactants distribution is mainly defined by the flow-field design [27]. Therefore, various investigations have been conducted to design and optimize the geometry and the material of bipolar plates. However, most of the published studies on flow-field effects considered a normal operating temperature [28–31], and only a very limited number of studies discussed the effects of flow and transport problem on cold start process [32]. Santamaria et al. [33] carried out an experimental study to investigate the interdigitated flow field and parallel flow field at different current densities under less extreme cold start in the range of −10 °C–0 °C using galvanostatic start-up. Their results showed that the interdigitated flow field has an enhanced water removal from cathode CL, thus it exhibits a better performance under less extreme cold start. On the other hand, in practical PEMFC stack applications the amount of supplied reactants to each channel is not the same, and it greatly depends on the inlet position of reactants as well as the flow distributor design [34,35], resulting in non-uniform inflow rate profile, which indirectly affects the local distributions of key parameters such as current density and water production amount. However, the effect of non-uniform inflow is simplified and neglected in most of the previous cold start modeling studies.

The coolant flow rate is one of the key parameters to obtain a better cold start performance. Practically, the coolant flow rate can be adjusted by controlling the coolant circulation pump. Recently, Wei et al. [36] numerically investigated the effect of coolant flow rate on the cold start performance. Three coolant flow rate values: 20, 40, 80 LPM (liter per minute), were considered for the fuel cell stack. Applying a high coolant flow rate of 80 LPM was found to result in more even temperature distribution in the cell due to the faster circulation of coolant, to some extent, beneficial to the cold start operation. However, increasing the flow rate of coolant to 80 LPM leads to more heat to be carried away by the coolant, thus requires more time to warm up the cell and consequently prolongs the startup time.

In this paper, a multidisciplinary, multi-channel cold start model is presented to accurately elucidate the effect of non-uniform distribution of reactants/coolant inflow on the cold start behavior. The model is then validated by cold start experiment data that given by SAIC Motor [37]. The model considers the coolant circulation effects on cold start performance. The influence of key operating parameters such as initial water content in membrane and cathode stoichiometry is analyzed under non-uniform reactants/coolant inflow profiles to provide information and guidance for an optimum operating cold start strategy.

Numerical model

A schematic description of the PEMFC computational domain is presented in Fig. 1. The geometry is based on the practical common PEMFC with all fundamental components, i.e. gas channels (GCs), bipolar plates (BPs), cooling channels (CCs), gas diffusion layers (GDLs), catalyst layers (CLs), and a membrane. The proposed geometry is purposely designed to enable the investigations of coolant/reactants inflow maldistribution in PEMFC channels. In order to minimize the computational cost and time, only half-cell model consisting of five parallel flow channels and all the sub-components of PEMFC is considered and parallel computation methodology is applied as well.

The present multi-channel model is developed based on our recent work [36], and the following assumptions were made:

- All the gas species obey the ideal gas law.
- The fluid is assumed to be incompressible due to the small pressure gradients in flows.
- The GDLs and CLs are considered as isotropic and homogeneous porous layers.
- The water vapor will instantaneously de-sublimate at saturation.
- The reactants and coolant flow rates are treated corresponding to the location of the inlet and outlet of flow channels.
- The temperature is assumed to be uniform in the cooling tank.

PEMFC cold start model

Besides the above-mentioned assumptions, this present cold start model fully accounts for the transient multiple transport

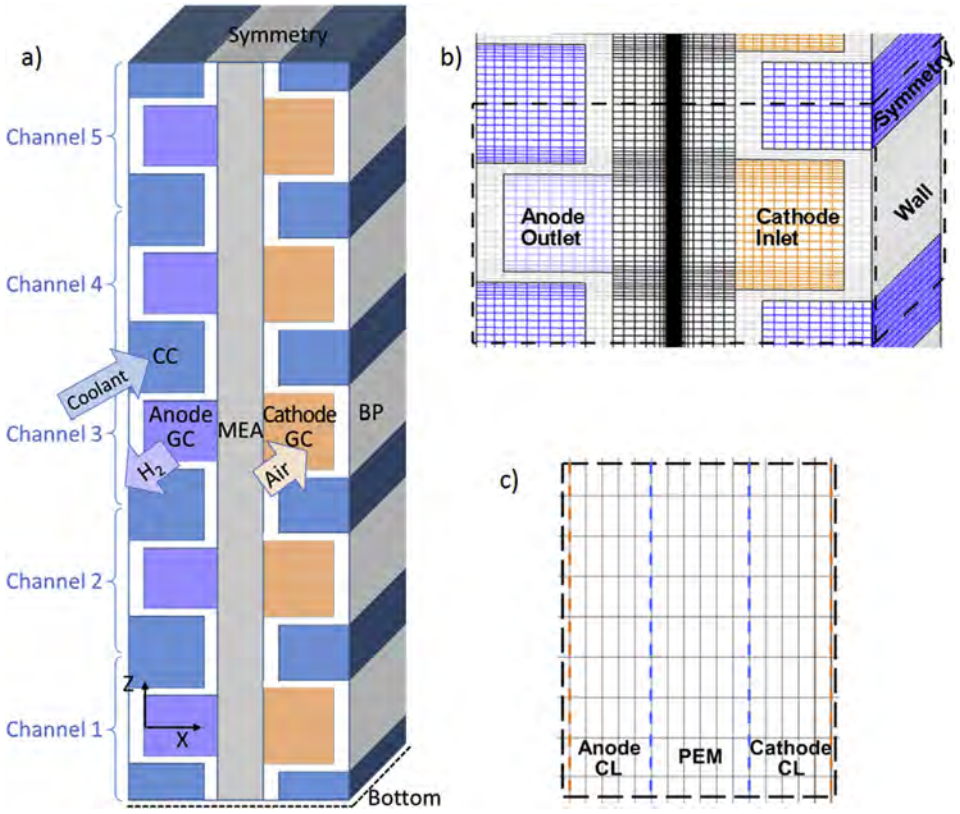

Fig. 1 – Computational domain and mesh of a PEMFC (channels are marked as channel 1 to channel 5 from the bottom cell to the middle cell).

and electrochemical process occurring in the parallel flow field fuel cell. The model is formulated based on the conservation equations of mass, momentum, species, charge, and energy as follows.

Mass conservation:

$$\frac{\partial(\varepsilon_s\rho_s)}{\partial t}+\frac{\partial(\varepsilon\rho)}{\partial t}+\nabla\cdot(\rho\vec{u})=0 \tag{1}$$

Momentum conservation:

$$\frac{1}{\varepsilon}\left[\frac{\partial(\rho\vec{u})}{\partial t}+\frac{1}{\varepsilon}\nabla\cdot(\rho\vec{u}\vec{u})\right]=-\nabla p+\nabla\cdot\tau+S_u \tag{2}$$

Species conservation:

$$\frac{\partial(\varepsilon C_k)}{\partial t}+\nabla\cdot(\vec{u}C_k)=\nabla\cdot\left(D_k^{eff}\nabla C_k\right)+S_{C,k} \tag{3}$$

Charge conservation:

For proton transport

$$\nabla\cdot\left(\kappa^{eff}\nabla\varphi_e\right)+S_{\varphi,e}=0 \tag{4}$$

For electron transport

$$\nabla\cdot(\sigma\nabla\varphi_s)+S_{\varphi,s}=0 \tag{5}$$

Energy conservation:

$$\frac{\partial(\rho c_p T)}{\partial t}+\nabla\cdot(\rho c_p\vec{u}T)=\nabla\cdot\left(k^{eff}\nabla T\right)+S_T \tag{6}$$

The source terms of governing equations for PEMFC cold start [38] are summarized in Table 1. In the mass continuity equation, the influence of the consumption/formation of reactants/product on the flow characteristics is negligible [39]. The source term of momentum equation in GDLs and CLs are described by Darcy's law.

The general species conservation equation for hydrogen, oxygen, vapor, and water vapor are given in terms of molar concentration. The species source terms account for:

- The produced water in the cathode CL due to the ORR, which is proportional to the volumetric transfer current density j.
- The effects of electro-osmotic drag on water transport in PEM and CL.
- The phase change. In the CLs and GDLs, we assume that there is no liquid water existing, but a direct phase transition from vapor water to solid ice [20,38,40]. This means when the vapor concentration reaches the saturation value, it will instantaneously de-sublimate. Therefore, the phase change source term in water conservation equation can be calculated by

$$S_{ice}=\begin{cases}0, & C^{H_2O}\le C_{sat}^{H_2O}\\ r_{freeze}\left(C_{sat}^{H_2O}-C^{H_2O}\right), & C^{H_2O}>C_{sat}^{H_2O}\ and\ T<T_{freeze}^{H_2O}\\ r_{melt}\left(C_{sat}^{H_2O}-C^{H_2O}\right), & T=T_{freeze}^{H_2O}\ and\ s>0\\ 0, & T\ge T_{freeze}^{H_2O}\ and\ s=0\end{cases} \tag{7}$$

Table 1 – Source terms for PEMFC cold start model.

	GDL	CL	PEM	BP	CC
Mass	0	0	0	/	0
Momentum	$S_u = -\frac{\mu}{K}\vec{u}$	$S_u = -\frac{\mu}{K}\vec{u}$	/	/	0
*Species	$S_C = -S_{ice}$	$S_C = -\frac{s_k j}{nF} - \nabla\cdot\left(\frac{n_d}{F} i_e\right) - S_{ice}$	$S_C = -\nabla\cdot\left(\frac{n_d}{F} i_e\right)$	/	/
Charge	/	$S_{\varphi,e} = j$	0	/	/
	0	$S_{\varphi,s} = -j$	/	0	/
Energy	$S_T = \frac{i_s^2}{\sigma} + h_{sg} S_{ice}$	$S_T = j\left(\eta - T\frac{dU_0}{dT}\right) + \frac{i_e^2}{\kappa^{eff}} + \frac{i_s^2}{\sigma} + h_{sg} S_{ice}$	$S_T = \frac{i_e^2}{\kappa^{eff}}$	$S_T = \frac{i_s^2}{\sigma}$	0

*The electro-osmotic term is only applied for water in ionomer phase, and S_{ice} is for H_2O transport only.

where, r_{freeze} and r_{melt} are phase change rates for freezing and melting, respectively. The freezing rate is assumed to be sufficiently large to make C^{H_2O} very close to $C_{sat}^{H_2O}$ regarding to the assumption of instantaneous de-sublimation at saturation. The melting rate is calculated by the energy conservation equation by fixing the temperature at the freezing point until all the ice is melt.

The effective species diffusion coefficient D_k^{eff} in species conservation equation is modified by Bruggeman correlation to account for the effects of porosity and tortuosity of porous layers (GDL/CL) [21], as follows:

$$D_k^{eff} = D_k \varepsilon^n \tag{8}$$

The blockage of species diffusion caused by ice formation in porous layers can be simply corrected by ice fraction s, that is:

$$D_k^{eff} = D_k[\varepsilon_0(1-s)]^n \tag{9}$$

where ε_o is the intrinsic porosity and the ice fraction s is defined as the volume ratio of ice to the pores in the CL.

$$s = \frac{V_{ice}}{V_{pore}} \tag{10}$$

While the water diffusivity in the membrane phase and the gas phase are expressed by Eq. (8) and Eq. (9), respectively:

$$D_g^{H_2o} = D_o\left(\frac{T}{353.15}\right)^{\frac{3}{2}}\left(\frac{P_o}{P}\right) \tag{11}$$

$$D_{mem}^{H_2o} = \begin{cases} 3.1\times10^{-5}\lambda\left(e^{0.28\lambda}-1\right)e^{\left(-\frac{4269}{T}\right)} & if\ 0<\lambda\le 3 \\ 4.17\times10^{-6}\lambda(1+161e^{-\lambda})e^{\left(-\frac{4269}{T}\right)} & else \end{cases} \tag{12}$$

The source terms in the charge conservation equations $S_{\varphi,s}$ and $S_{\varphi,e}$ present the electrochemical-reaction kinetics in CLs, i.e. the oxygen reduction reaction (ORR) in the cathode side and the hydrogen oxidation reaction (HOR) in the anode side. The generated transfer current density distribution in CLs based on simplified Butler-Volmer equation can be described as:

$$j_a = a i_{0,ref}^{H_2}\left(\frac{C^{H_2}}{C_{ref}^{H_2}}\right)^{1/2}\exp\left(\frac{\alpha_a+\alpha_c}{RT}F\eta\right) \tag{13}$$

$$j_c = -a i_{0,ref}^{O_2}\frac{C^{O_2}}{C_{ref}^{O_2}}\exp\left(-\frac{\alpha_c}{RT}F\eta\right) \tag{14}$$

where the surface overpotential η is defined as

$$\eta = \Phi_s - \Phi_e - U_0 \tag{15}$$

In the energy conservation equation, heat source term may contain the entropic heat, irreversible electrochemical heat, ohmic heat, and latent heat.

Numerical implementation and boundary/initial conditions

The presented cold start PEMFC model in Section PEMFC cold start model is numerically implemented using the commercial CFD (Computational Fluid Dynamics) software, Fluent©. Therefore, the conservation equations along with the boundary conditions and initial conditions are specified in the user code using the code's user defined functions (UDFs). The grid and time-step sizes for various cold start simulation cases of this study were determined based on the grid-independence study performed by Wei et al. [36]. Due to the symmetrical structure, only half of the multi-channel cell is considered to reduce the computational time. The model also considers the coolant effects by developing cooling channels on the shoulder of BP at both anode and cathode sides.

The reactants concentrations at GC inlets are specified as constant values, while the temperature of the inlet gas is equal to that of the environment. A reference electronic phase potential (zero) is set at the anode side and a constant flux (current density loading) at the cathode wall, so that the calculated electron phase potential on the cathode wall would be the cell output voltage. Zero-flux boundary condition is also applied to the electrolyte phase. All the other external boundaries are assumed to be zero-flux for all the other main variables not mentioned above.

The initial temperature for the whole PEMFC is set as that of the environment. The reactant species in GCs and GDLs are initially set to have the same molar concentration as the inlet gas. For most of the cases, before the cold startup, it is assumed that a sufficiently long purge with a fixed relative humidity value has been performed that the initial water content in ionomer phase in CLs and in PEM is constant. For example, if the relative humidity of the purge gas is 50%, the initial water content in ionomer phase in CLs and in PEM is $\lambda_0 = 3.3$ [19]. The initial ice fraction in the cell is assumed zero [20].

The cell dimensions and materials properties are listed in Table 2 and Table 3, respectively. The proton conductivity in the membrane, κ is given by Eq. (16) [19]as:

$$\kappa = (0.5139\lambda - 0.326)\exp\left[2222\left(\frac{1}{303} - \frac{1}{T}\right)\right] \quad (16)$$

Fig. 2 shows the reactants and coolant distribution through the different neighboring channels. The plotted data of reactants/coolant inflow profiles were experimentally performed by SAIC Motor. The locations of the distributor and the manifold (both the inlet and outlet locations), which are not shown in this figure, induce the curved uneven profiles. As can be seen, the flow rate distribution of coolant/reactants is dependent on the channeling length. Therefore, the highest flow rate exists on the channel with the shortest distance between the inlet and outlet, while the flow rates values of the gases/coolant channels with the long travelling path are dramatically declined mainly because of the large flow resistance along the pathway from the channel inlet to outlet.

The average inflow velocities in anode and cathode flow channels can be calculated from the stoichiometric flow ratio as:

$$u_{in,a} = \frac{\xi_a \frac{I}{2F} A_{mem}}{C_{H_2} A_{a,GC}}, \quad u_{in,c} = \frac{\xi_c \frac{I}{4F} A_{mem}}{C_{O_2} A_{c,GC}} \quad (17)$$

And the inflow velocities of both gases and coolant for each channel are defined as:

$$u_{n,gas} = u_{in}\left[0.9934\left(\frac{n}{n_{tot}}\right)^2 - 1.006\left(\frac{n}{n_{tot}}\right) + 1.1825\right] \quad (18)$$

$$u_{n,coolant} = u_{in}\left[-1.6144\left(\frac{n}{n_{tot}}\right)^2 + 1.5491\left(\frac{n}{n_{tot}}\right) + 0.6953\right] \quad (19)$$

where n is the number of channel and n_{tot} is the total number of channels.

Results and discussion

In this study, different current loading procedures were applied to adopt a similar loading rate as applied in the experiments. In the first 8 s the current load is gradually increased every 2 s, which aims to hydrate the initially dry membrane and increase the heat generation rate to create the cell temperature rise, thus accelerating the cell warm-up, and then the fuel cell operated under constant current load condition mainly to avoid excessive ice formation in the CL [9,18].

Table 2 – Cell dimensions.

Description	Value
Cell length	0.28 m
Width of anode/cathode GC	0.9/1.2 mm
Width of anode/cathode CC	1.1/0.8 mm
Depth of GC	0.4 mm
Thickness of BP (δ_{BP})	0.1 mm
Thickness of GDLs (δ_{GDL})	0.2 mm
Thickness of CLs (δ_{CL})	0.015 mm
Thickness of PEM (δ_{mem})	0.018 mm

Table 3 – Materials properties.

Description	Value	Units
Porosity of GDL/CL ($\varepsilon_{GDL}/\varepsilon_{CL}$)	0.51/0.40	
Permeability of the GDL/CL (K_{GDL}/K_{CL})	6.1×10^{-12}	m^2
Electronic conductivity in BP (σ_{BP})	1.4×10^6	S m^{-1}
Electronic conductivity in GDL/CL (σ_{GDL}/σ_{CL})	300	S m^{-1}
Thermal conductivity of BP (k_{BP})	16	W m^{-1} K^{-1}
Thermal conductivity of GDL/CL (k_{GDL}/k_{CL})	1.7/0.27	W m^{-1} K^{-1}
Thermal conductivity of PEM (k_{mem})	0.16	W m^{-1} K^{-1}
Thermal conductivity of coolant ($k_{coolant}$)	0.25	W m^{-1} K^{-1}
Thermal mass of BP ($\rho c_{p,BP}$)	4000	kJ m^{-3} K^{-1}
Thermal mass of GDL/CL ($\rho c_{p,GDLl}/\rho c_{p,CL}$)	230/580	kJ m^{-3} K^{-1}
Thermal mass of PEM ($\rho c_{p,mem}$)	2300	kJ m^{-3} K^{-1}
Thermal mass of coolant ($\rho c_{p,coolant}$)	3400	kJ m^{-3} K^{-1}
Diffusivity of H_2/O_2 in gas (D_{H2}/D_{O2})	$8.67 \times 10^{-5}/1.53 \times 10^{-5}$	m^2 s^{-1}
Diffusivity of vapor in gas (D_{vapor})	1.79×10^{-5}	m^2 s^{-1}
Dry membrane density (ρ_{mem})	1980	kg m^{-3}
Equivalent weight of electrolyte in PEM (EW)	1.0	kg mol^{-1}

The initial water content is 3.0, the stoichiometry values in the cathode and anode sides are 3 and 2.89, respectively. The initial ice fraction is 0 in the cathode CL. The cold start modeling results have been compared with the experimental results for cases starting from sub-zero temperature of −20 °C. The operating conditions in the proposed multi-channel model are defined corresponding to the experiments in Refs. [37]. More detailed descriptions of the cell stack experiments

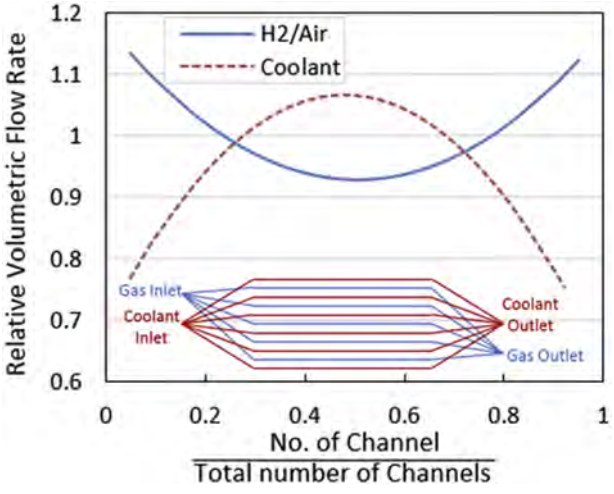

Fig. 2 – The flow rate distribution of reactants and coolant in a practical PEMFC stack.

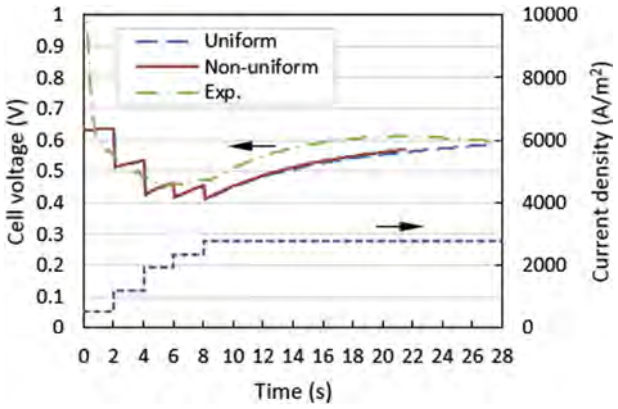

Fig. 3 – Comparison between the model prediction and experimental data [36,37].

can be found in our recent work in Ref. [36]. The simulated results are found to be in good agreement with the experimental data as shown in Fig. 3, indicating the validity of the presented cold start model. The uniform and non-uniform cases (case 1 and case 2) are shown to have cell voltage curves with little difference.

The results of this work are presented and discussed in three sub-sections: the first sub-section (Section Cold start behavior under varied flow rates) explores the cold start behaviors of the newly developed parallel multi-channel model, including cell voltage performance, temperature distribution, and ice formation. In the second and third sub-sections (Section Effect of initial water distribution and Section Effect of flow stoichiometry), we investigate the influence of key parameters such as the initial membrane water content and cathode stoichiometry ratio on cold start process in term of ice formation rate and current density distribution. Therefore, five simulation cases were conducted in this study as presented in Table 4.

Cold start behavior under varied flow rates

All the simulated cases achieved a successful self startup, thereby they stopped when the temperature reaches 0 °C. Fig. 3 shows that the multi-channel cell could realize a rapid startup from subzero temperature of −20 °C, it also shows that it takes 21 s for the multi-channel cell with non-uniform inflow (Case 2) to reach 0 °C and 27 s when uniform inflow (Case 1) was applied. Although the startup time of one case prolongs, the voltage output exhibits no noticeable change. To gain more insight into the internal behavior of cold start process under both uniform and non-uniform applied inflow rates, the characteristics of temperature and ice formation for multi-channel cells are explored in this section.

Fig. 4 displays the temperature profiles along the z-line crossing the middle of cathode outlet at different time instants of 13s, 17s, and 21s, respectively, for Case 1 and Case 2. The highest temperature gradient over the cold start duration is found to be in Case 2 (non-uniform case) at the first channel (end channel) and slightly decreased from the first channel to the fifth channel (middle channel) mainly due to the varied inflow rates of reactants/coolant in different channels. The reactants inflow rate is an important factor that determines the reaction intensity distribution in the cathode CL. Therefore, the higher flow rate of reactants in the end channels improves their reaction rate and promotes the temperature rise. In addition, the fifth channel of Case 2 shows the lowest temperature difference over cold start duration owing to its higher coolant flow rate [36], indicating that middle channels have more even temperature distribution compared with end channels. In contrast, the temperature distribution in the uniform inflow rate case (Case 1) with constant relative volumetric flow rate of 1 shows no much difference between the neighboring channels. Interestingly, a comparison of the temperature profiles of the two cases releases that the higher reactant flow rate of the end channels in Case 2 progressively promotes the temperature rise as we can see in Fig. 5, while the higher coolant flow rate in the middle channel of Case 2 lowers the temperature rise rate in this channel, signifying the importance of considering the effect of non-uniform inflow rate in future cold start simulation.

Fig. 6 depicts the ice fraction profiles along a z-line at the middle of cathode CL in Case 1 and Case 2. As can be seen in Fig. 6, the regions under the lands of individual channel part show larger amount of ice formation compared with the region under gas flow channels. That is mainly because the higher water transfer resistance and lower electric transport resistance (which means higher current density) in the region under-lands [36]. Furthermore, the peak of ice formation is shown toward the end channels for Case 2, which may be caused by the higher reactants flow rate in these channels, and consequently stronger reaction intensity and higher water production rate. To conclude from Figs. 4–6, the coolant flow rate contributes to affect the ice formation and

Table 4 – Simulation cases.

Case #	Initial water (λ)	Cathode CL Stoichiometry ratio (ξ_c)	Comments/Purpose of the case	The operating flow rate of reactants/coolant
Case 1	3.0	3.0	Uniform inflow profile	H_2 = 0.02 LPM
Case 2	3.0	3.0	Non-uniform inflow profile	Air = 0.05 LPM
Case 3	5.0	3.0	Non-uniform inflow profile and higher initial membrane water content	Coolant = 0.02 LPM (these values for the single cell and they are used in all the cases)
Case 4	Average (4.1)	3.0	Non-uniform inflow profile with uneven initial water content	
Case 5	3.0	1.2	Non-uniform inflow profile and Low Stoichiometry operating condition	

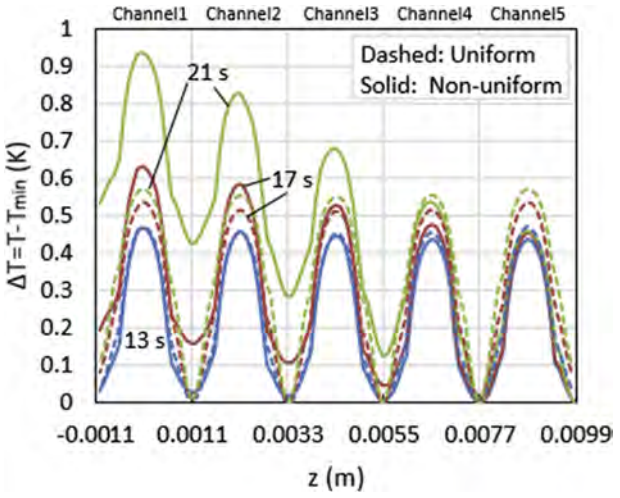

Fig. 4 – Cell temperature profiles along the z-line crossing the middle of cathode outlet in Case 1 and Case 2. T_{min} denotes the minimum temperature on the line.

temperature distribution, however, the effect of reactants flow rate profile is more dominant during the cold start process. It is noteworthy that there is little difference at the ice fraction profiles between different channel parts for Case 1, as expected.

The ice formation, water uptake in CL and membrane share the same generated water. Fig. 7 shows the water balance map of the first and fifth gas flow channels during the cold start of case 2. The positive and negative values represent water generation and water consumption in cathode CL, respectively. The generated water mainly goes to the membrane and the ionomers in cathode CL [38]. The accumulated water in cathode CL starts to freeze once the water content reaches the maximum and the water vapor is fully saturated. The water balance map does not show big difference between the two channels. The water balance of Case 1 is not presented here because it is very similar to Case 2. However, the water production rate is found to be equivalent with the water removal rate in terms of ice formation or accumulated water in CL and membrane, to a great extent, verifying the accuracy of the presented multi-channel model.

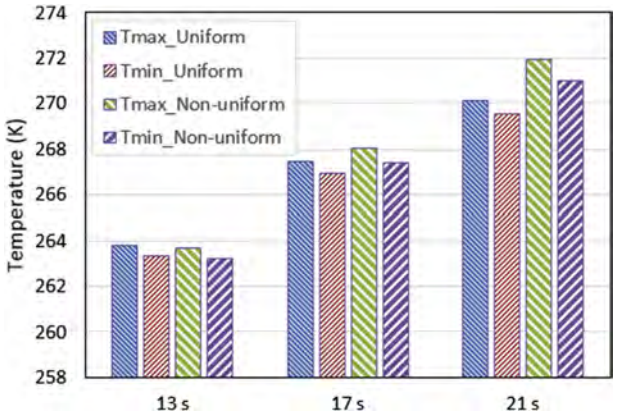

Fig. 5 – Maximum and minimum temperature values on the z-line crossing the middle of cathode outlet at time instants of 13s, 17s, and 21s in Case 1 and Case 2.

Effect of initial water distribution

On the early stage of cold start process (before the ice start to form) the cell operating voltage is dominated by the proton conductivity of the membrane [41]. To maintain high proton conductivity, the membrane needs to be hydrated [42]. Therefore, the membrane water content determines the proton conductivity and thus influences the cold start performance [12]. In this section we investigate the impact of initial water content on the cold start process using the present multi-channel cell model with non-uniform reactants/coolant inflow profiles. Three initial water content values of $\lambda_0 = 3$, $\lambda_0 = 5$, and varied-value content (where $\lambda = 4.1$ as average value) are considered, corresponding to Case 2, Case 3, and Case 4, respectively. Case 4 aims to capture the uneven distribution of initial water content in the membrane after purge. Normally, larger amount of water accumulates under the lands region than under the gas flow channels. Hence, an initial water content of 3 is assumed under gas flow channel region for all channels. On the other hand, the membrane water content value under the land region is gradually increased from 4 (in the first channel) to 6 (in the fifth channel). The average value of initial water content in Case 4 is 4.1.

Fig. 8 compares the cell voltage evaluation curves of Cases 2, 3, and 4. The three cases were started up successfully. Case 3 ($\lambda_0 = 5$) shows a considerable increase in the output cell voltage in both early and latter stages of the cold start process. This is mainly due to its enhanced proton conductivity under the higher initial membrane water content and consequently its lower ohmic losses for proton transportation in the membrane and catalyst layers.

Fig. 9 shows the current density distribution in the membrane of the multi-channel cell at different time instants of 3 s,

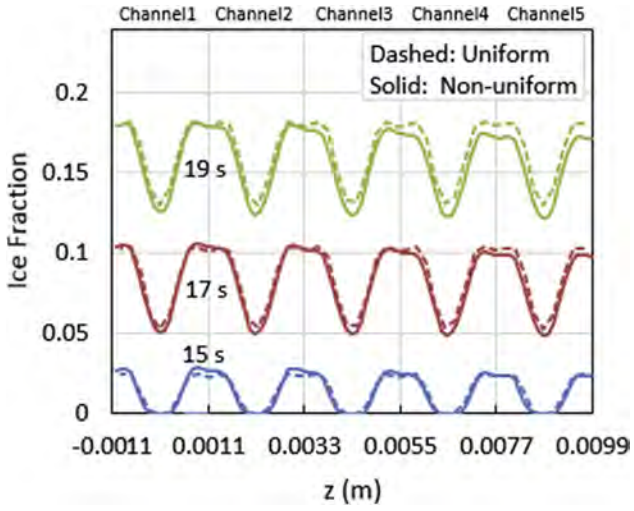

Fig. 6 – Effects of non-uniform inflow rates of reactants/coolant on the ice formation in cathode CL of Case 1 and Case 2. The monitoring line is a z-line at the middle of cathode CL.

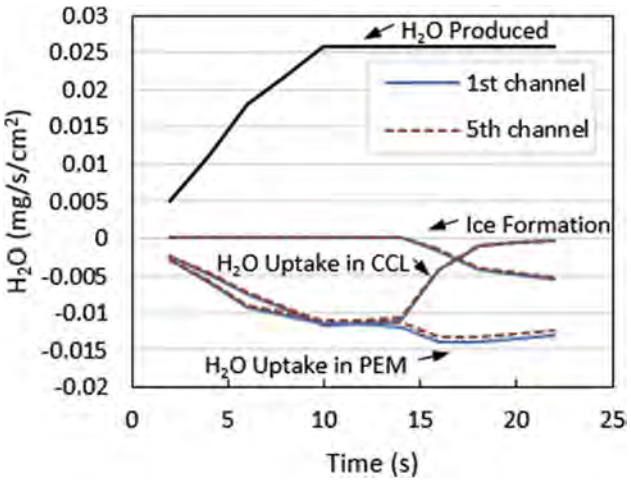

Fig. 7 – Evaluation of water balance of the 1st and 5th channels during case 2 cold start process.

9 s, and 15 s for Cases 3 and 4. The current density contours obviously show that the non-uniform initial water content case (Case 4) has an evidently enlarged range of current density values at time instants of 3 s and 9 s compared to Case 3, demonstrating the stronger non-uniformity effects in Case 4.

In Case 3, the current density is higher under land due to the higher electric conductivity therein. At early stages of cold start (i.e. t = 3s), along the flow direction, the current density decreases due to the oxygen consumption. While among the channels along z-axis, the first channel exhibits the highest current density distribution. The current density distribution slightly decreases from the first channel toward the fifth channel along z direction, which is mainly due to the decreased inflow rate of reactants, indicating that the reactant flow rate and electric conductivity are the dominant factors for determining the current density in Case 3. At the latter stages of cold start of Case 3, the high current density distribution region is shifted from the inlet region to the intermediate region and finally to the outlet region along the flow direction. This relocation of current density distribution is related to the water and heat production, and the ice formation. A similar trend was found in Ref. [36,43].

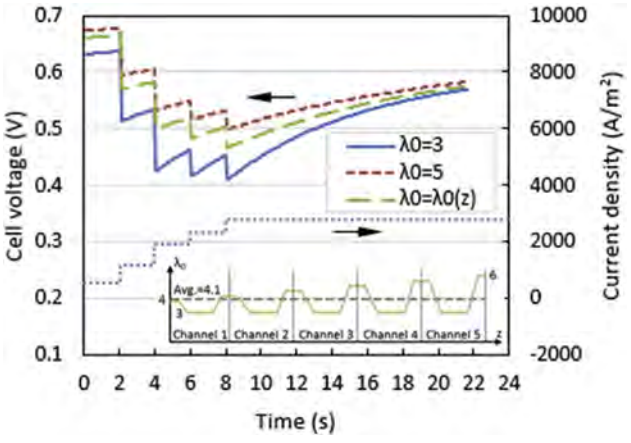

Fig. 8 – Cell voltage evolution curves for Cases 2–4.

In Case 4, a non-uniform initial water content distribution is implemented. The current density is higher in the region under land. In contrast to Case 3, the highest current density distribution is located in the fifth channel due to the highest initial water content ($\lambda_0 = 6$ under land), indicating that the current density distribution between channels is mainly determined by the degree of the membrane hydration in Case 4, while the reactant inflow rate distribution has no much influence on the current density distribution among individual channels, as it appears in Fig. 9. At the latter stages of cold start, the higher coolant flow rate in the fifth channel results in more even current density distribution in Case 4, which is consistent with the results obtained in Ref. [36].

Fig. 10 depicts the ice formation and distribution in the cathode CL at time instants of 15 s and 21 s for Cases 3 and 4. The ice fraction grows faster in the region under the land due mainly to the higher current density therein. It is found that the contour plots of Case 4 show more non-uniform ice formation with the highest ice fraction value in the 5th channel region.

To sum up, the non-uniform inflow rates of reactants and coolant under various applied initial membrane water content show different current density and ice formation distributions. The non-uniformity of initial water content in membrane may significantly change the pattern of the effects of non-uniform inflow rates of reactants and coolant.

Effect of flow stoichiometry

The stoichiometry is a key parameter influencing PEMFCs performance [44]. A high stoichiometric ratio results in an enhanced reactants transport rate. However, too high stoichiometric ratios may cause membrane dehydration. On the other hand, a further decrease of stoichiometric ratio promotes the water flooding [45]. A recent study investigated the impact of cathode stoichiometry on normal PEMFCs performance [46]. It is found that using a suitable cathode stoichiometry benefits to prevent both the membrane dehydration in the near inlet region and flooding in the near outlet region. The cathode stoichiometry is usually supplied under the range of 1.5–3.0 [47,48]. Two different stoichiometry factors for oxygen are considered in order to examine the cold start performance under varied reactants/coolant supplying conditions. Fig. 11 shows the cell voltage at stoichiometric coefficients of 1.2 (Case 5) and 3 (Case 2) under cold start temperature of −20 °C. It is clearly seen that increasing the stoichiometry factor from 1.2 to 3 results in a slight increase of the cell output voltage due mainly to the improved oxygen transport rate in the cathode CL under higher stoichiometry factor [49].

Fig. 12 demonstrates the oxygen concentration along the flow direction for Cases 2 and 5 at time instant of 15 s. The oxygen concentration gradually decreases along the flow path for both cases due to the oxygen consumption by the cathode electrochemical reaction. It is clearly seen that the oxygen

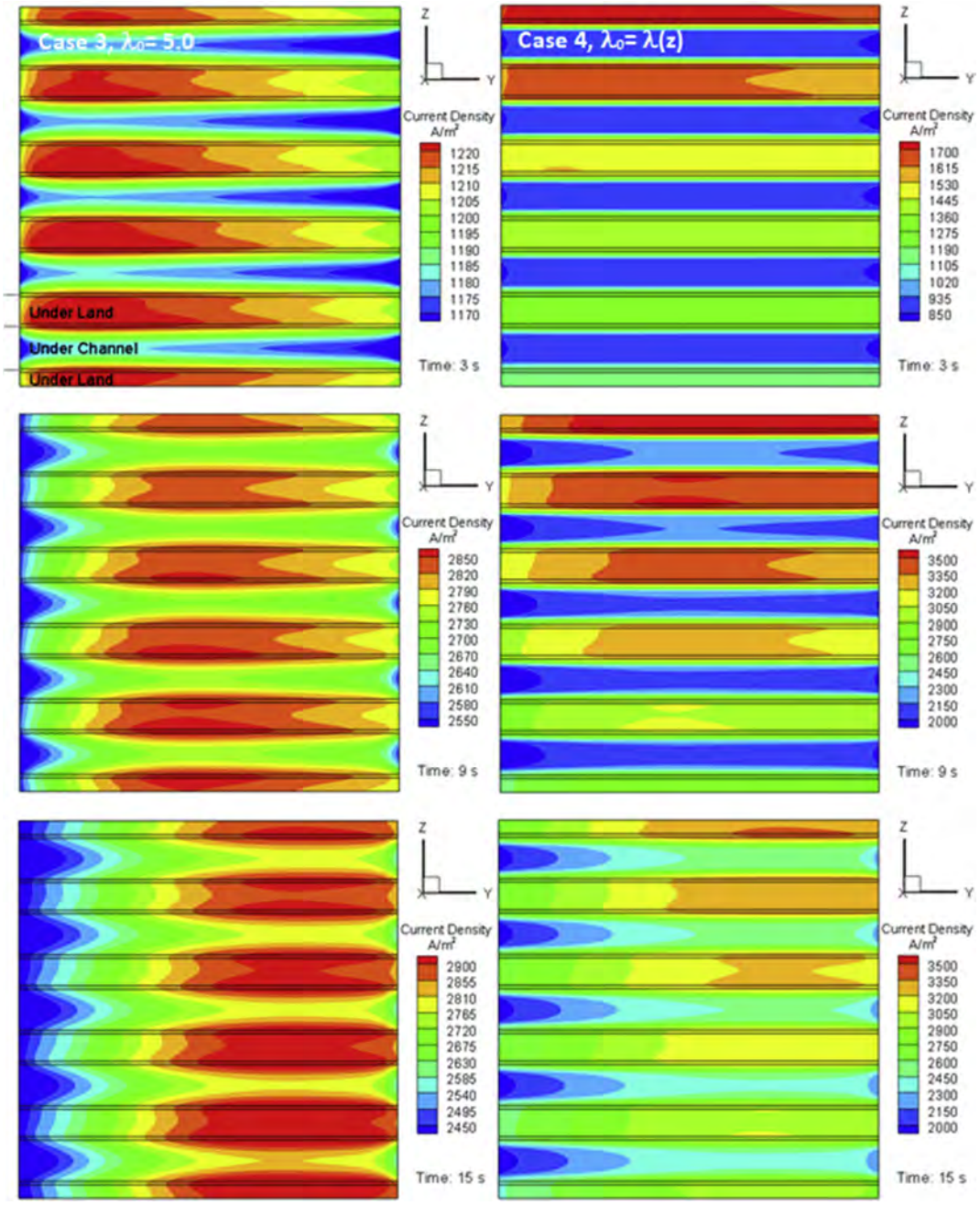

Fig. 9 – Current density contours in the membrane for Cases 3 and 4 at various time instant of 3 s, 9 s, and 15 s. The monitoring plane is the yz plane in the middle of the membrane.

concentration in Case 5 (with lower stoichiometry factor) shows a sharper decrement than Case 2, which may affect the current density distribution. In addition, the oxygen concentration in the fifth channel is found to be slightly lower compared with the first channel, in accordance with the applied flow rate boundary conditions.

Fig. 13 describes the current density distribution in the membrane central yz-plane for Cases 2 and 5 at different time instants of 9 s, 15 s and 21 s. It is obvious that the current density is clearly influenced by the oxygen concentration of each channel. Accordingly, the first and second channels show higher current density distributions.

In comparison of Case 2 and Case 5, during the cold start survival time of the two cases, the higher current density distribution region is shifted from the near inlet to the near outlet region. Besides that, at t = 15–21 s in the two cases, we can observe that the current density is clearly decreased toward the inlet, practically under GCs, and the decrement is more critical in Case 2. This behavior may be due to the high speed gas flow [46] and lower gas temperature at the inlet

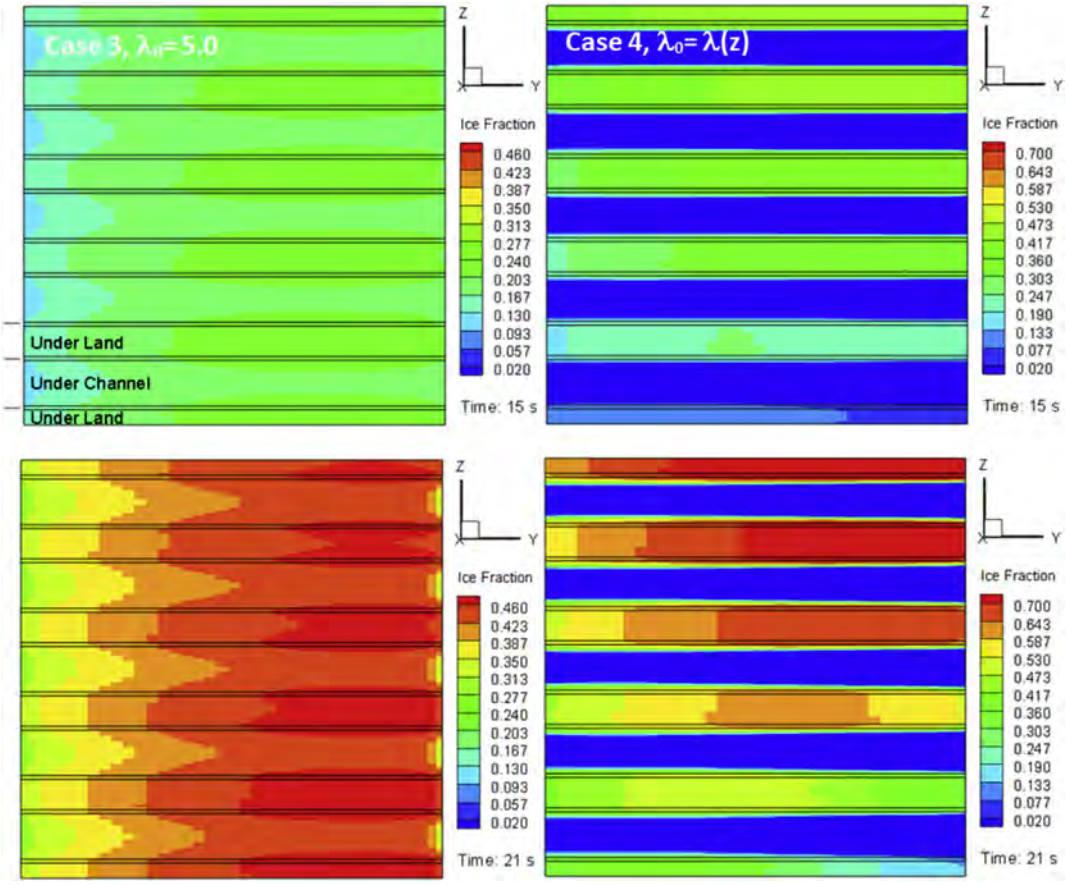

Fig. 10 – Ice fraction contours in the cathode CL for Cases 3 and 4 at time instants: 15 s and 21 s. The monitoring plane is the yz plane in the middle of the cathode CL.

region during last stages of cold start, and thus it is more critical under higher stoichiometry factor (Case 2). Also the effect of flow rate can be recognized through the decreased current density distribution among different channels. Generally, the maximum current density is larger for Case 2 compared with Case 5, which is mainly owing to its better oxygen availability at cathode CL. The oxygen availability at cathode CL reduces the activation and concentration losses [44], thus results in a better fuel cell performance [50].

Fig. 14 displays the ice fraction distribution in the central yz-plane of cathode CL for Cases 2 and 5 at time instants of 15s

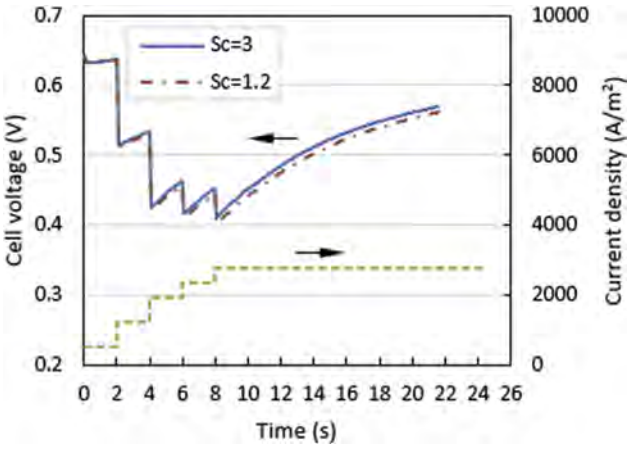

Fig. 11 – Comparison of cell voltage evolution curves in Cases 2 and 5.

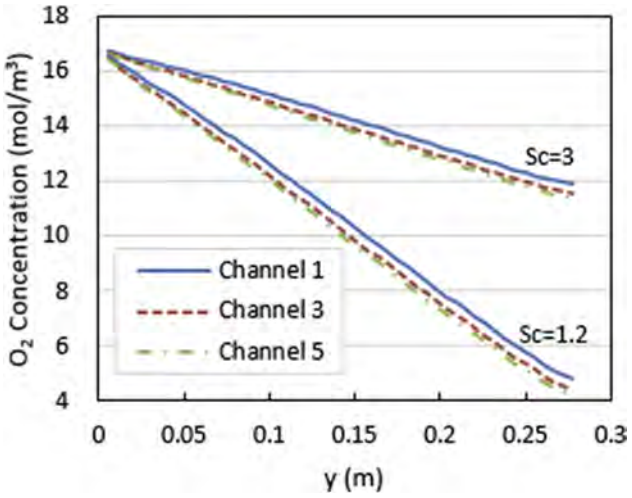

Fig. 12 – Oxygen concentration distributions in cathode CL along the flow direction for Cases 2 and 5 at t = 15 s. The monitoring y-line is in the middle of cathode CL of the corresponding channel part.

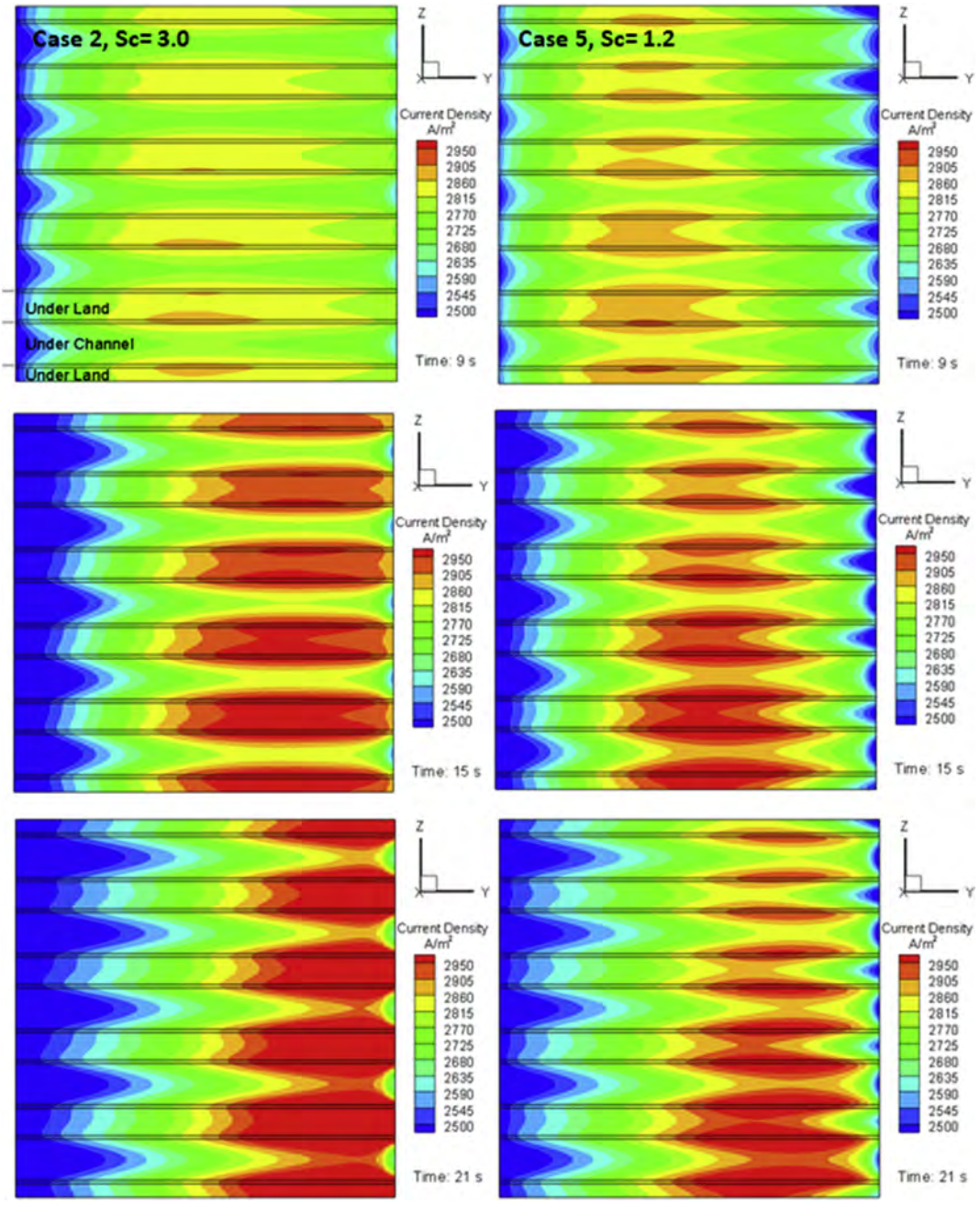

Fig. 13 – Current density contours in the membrane central yz-plane for Cases 2 and 5 at different time instant of 9 s, 15 s and 21 s.

and 21s. Although, Case 5 shows a relatively lower maximum current density in Fig. 13, the ice fraction growth is found to be slightly faster in both under land and under GC regions. This behavior occurs because the water removal capability by gas is relatively better in Case 2 owing to its larger stoichiometry ratio [45], hence slightly more water accumulation and ice formation appear in Case 5 compared with Case 2.

Finally, by increasing the stoichiometry factor from 1.2 to 3, the cold start performance is slightly improved. The case with higher stoichiometry factor (Case 2) is found to have higher current density distribution and lower ice formation rate, mainly due to its better oxygen availability to the cathode CL and higher water removal rate. However, it is found that the current density distribution in the region near the inlet is very low, particularly under GCs, which may result in less water production in this region, and thus ends up with drying of the membrane. The results indicate the importance of considering an adequate stoichiometry ratio that ensures more uniform current density distribution and prevent the drying of the membrane near the inlet region in order to achieve a better cold start performance of PEMFCs and prolong their life time.

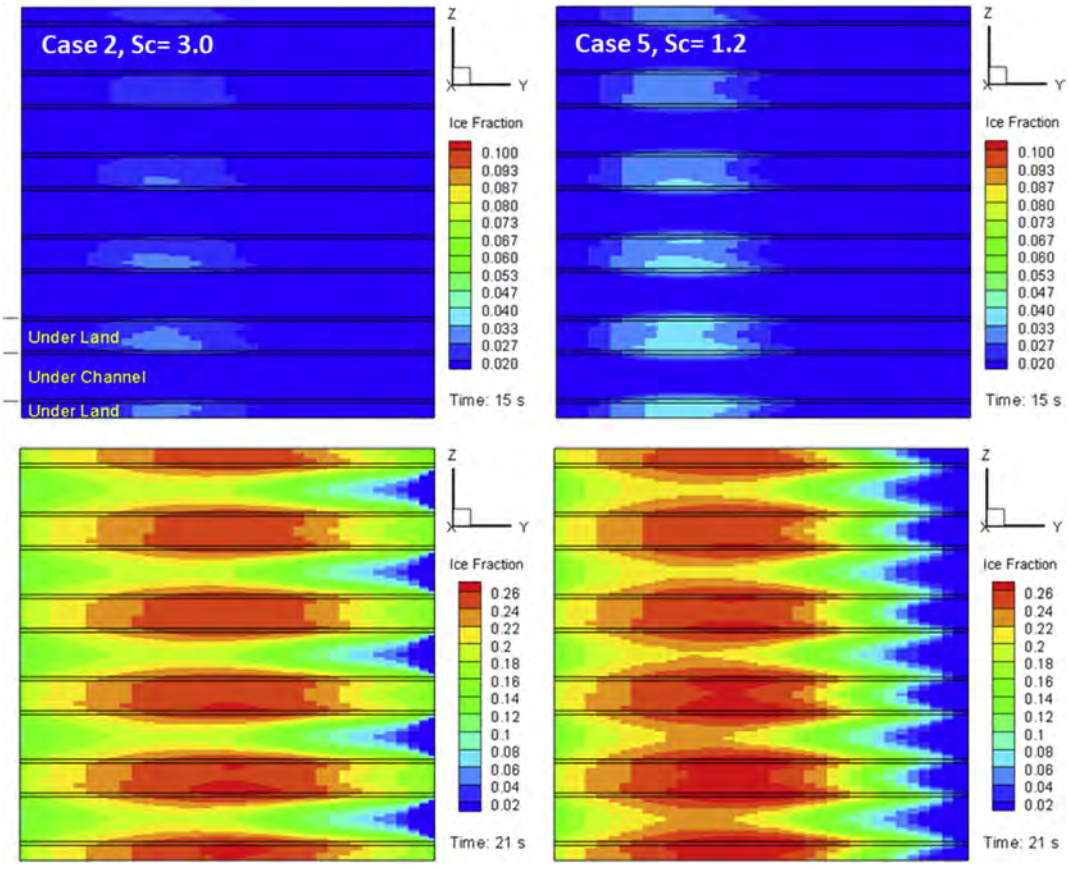

Fig. 14 – Ice fraction contours in the central yz-plane of cathode CL for Cases 2 and 5 at time instants of 15 s and 21 s.

Conclusions

The reactants and coolant distributions in PEMFC channels are crucial for PEMFC performance. In actual PEMFC stack applications the inflow rate for each channel greatly depends on the inlet position of reactants distributor and manifold. A three-dimensional, non-isothermal, multi-channel cold start model is developed to numerically investigate the effects of non-uniform inflow reactants/coolant flow rates on cold start process. The simulated and measured voltage curves were found in good agreement over the cold start duration, demonstrating the validity of the model. In addition, it is found that the reactants flow rate profile is more dominant during the cold start process. The channels share a similar water production and ice formation rates. However, the distribution uniformity of ice formation and current density is noticeably varied over the cold start duration. Furthermore, a detailed investigation was carried out to examine the effect of the initial membrane water content and stoichiometry ratio on cold start behaviors. The cell voltage performance, ice formation rate and current density distribution at different channels were presented and analyzed. We reported that after the purge process, the initial non-uniform water content in membrane may further worsen the uniformity of the formed ice and thus probably causing a serious damage to the structure of MEA. While higher cathode stoichiometry ratio improves the cold start capability due to the improved oxygen availability to the cathode CL, but may result in partially drying-out of the membrane close to the channel inlet region, and thus causes the performance degradation.

Acknowledgements

Financial support received from the China National Key R&D Project (2018YFB0905303), the Shanghai Automotive Industry Sci-Tech Development Foundation (No. 1706), and the Guangdong Science and Technology Department (2017B010120003, 2016A030313172, 2015A030308019) is gratefully acknowledged.

Nomenclature

A	Area; electrode area, m^2
C	Species concentration, mol m^{-3}
D	Diffusivity, m^2 s^{-1}
E	Elasticity modulus, MPa
EW	Equivalent weight of dry membrane, kg mol^{-1}
F	Faraday constant, C mol^{-1}
i	Current density, A m^{-2}
j	Transfer current density, A m^{-3}
K	Permeability, m^2

n_d	Electroosmotic drag coefficient
p	Pressure, Pa
$\dot{q}$	Water desublimation rate, mol m^{-3} s^{-1}
R	Universal gas constant, J mol^{-1} K^{-1}
s	Ice fraction
S	Source term
t	Time, s
T	Temperature, K
u	Superficial fluid velocity, m s^{-1}

Greek characters

ε	Porosity
λ	Water content in membrane
Φ	Phase potential, V
μ	Viscosity, Pa s
ξ	Stoichiometric flow ratio
ρ	Density, kg m^{-3}
η	Overpotential, V
κ	Proton conductivity, S m^{-1}

Superscripts/ Subscripts

a	Anode
c	Cathode
e	Electrolyte
eff	Effective
gs	Vapor-solid phase transition
k	Species index
mem	Membrane
o	Initial
ref	Reference value
s	Solid phase

REFERENCES

[1] Dafalla AM, Jiang F. Stresses and their impacts on proton exchange membrane fuel cells: a review. Int J Hydrogen Energy 2018;43:2327–48.

[2] Asghari S, Shahsamandi MH, Khorasani MRA. Design and manufacturing of end plates of a 5 kW PEM fuel cell. Int J Hydrogen Energy 2010;35:9291–7.

[3] Peighambardoust SJ, Rowshanzamir S, Amjadi M. Review of the proton exchange membranes for fuel cell applications. Int J Hydrogen Energy 2010;35:9349–84.

[4] Luo Y, Jiao K. Cold start of proton exchange membrane fuel cell. Prog Energy Combust Sci 2018;64:29–61.

[5] Ge S, Wang CY. Characteristics of subzero startup and water/ice formation on the catalyst layer in a polymer electrolyte fuel cell. Electrochim Acta 2007;52:4825–35.

[6] Nandy A, Jiang F, Ge S, Wang C-Y, Chen KS. Effect of cathode pore volume on PEM fuel cell cold start. J Electrochem Soc 2010;157:B726–36.

[7] Mao L. Thesis. Pensssylvania: The Pensssylvania State University, University Park; 2006.

[8] Mao L, Wang C. Analysis of cold start in polymer electrolyte fuel cells. J Electrochem Soc 2007;154:B139–46.

[9] Jiang F, Wang C-Y. Potentiostatic start-up of PEMFCs from subzero temperatures. J Electrochem Soc 2008;155:B743–51.

[10] Cho E, Ko J-J, Ha HY, Hong S-A, Lee K-Y, Lim T-W, et al. Characteristics of the PEMFC repetitively brought to temperatures below 0°C. J Electrochem Soc 2003;150:A1667–70.

[11] McDonald RC, Mittelsteadt CK, Thompson EL. Effects of deep temperature cycling on Nafion 112 membranes and membrane electrode assemblies. Fuel Cell 2004;4:208–13.

[12] Jiao K, Li X. Effects of various operating and initial conditions on cold start performance of polymer electrolyte membrane fuel cells. Int J Hydrogen Energy 2009;34:8171–84.

[13] Tajiri K, Tabuchi Y, Kagami F, Takahashi S, Yoshizawa K, Wang CY. Effects of operating and design parameters on PEFC cold start. J Power Sources 2007;165:279–86.

[14] Jiao K, Li X. Cold start analysis of polymer electrolyte membrane fuel cells. Int J Hydrogen Energy 2010;35:5077–94.

[15] Luo Y, Guo Q, Du Q, Yin Y, Jiao K. Analysis of cold start processes in proton exchange membrane fuel cell stacks. J Power Sources 2013;224:99–114.

[16] Dafalla AM, Wei L, Liao ZH, Jiang FM. Effects of clamping pressure on cold start behavior of polymer electrolyte fuel cells. Fuel Cell 2019;19:221–30.

[17] Ahluwalia RK, Wang X. Rapid self-start of polymer electrolyte fuel cell stacks from subfreezing temperatures. J Power Sources 2006;162:502–12.

[18] Jiang F, Wang C-Y, Chen KS. Current ramping: a strategy for rapid start-up of PEMFCs from subfreezing environment. J Electrochem Soc 2010;157:B342–7.

[19] Mao L, Wang C-Y, Tabuchi Y. A multiphase model for cold start of polymer electrolyte fuel cells. J Electrochem Soc 2007;154:B341–51.

[20] Ko J, Ju H. Comparison of numerical simulation results and experimental data during cold-start of polymer electrolyte fuel cells. Appl Energy 2012;94:364–74.

[21] Jiao K, Li X. Three-dimensional multiphase modeling of cold start processes in polymer electrolyte membrane fuel cells. Electrochim Acta 2009;54:6876–91.

[22] Meng H. Numerical studies of cold-start phenomenon in PEM fuel cells. Electrochim Acta 2008;53:6521–9.

[23] Sundaresan M, Moore RM. Polymer electrolyte fuel cell stack thermal model to evaluate sub-freezing startup. J Power Sources 2005;145:534–45.

[24] Khandelwal M, Mench MM. Direct measurement of through-plane thermal conductivity and contact resistance in fuel cell materials. J Power Sources 2006;161:1106–15.

[25] Zhou Y, Luo Y, Yu S, Jiao K. Modeling of cold start processes and performance optimization for proton exchange membrane fuel cell stacks. J Power Sources 2014;247:738–48.

[26] Lin R, Zhu Y, Ni M, Jiang Z, Lou D, Han L, et al. Consistency analysis of polymer electrolyte membrane fuel cell stack during cold start. Appl Energy 2019;241:420–32.

[27] Manso AP, Marzo FF, Barranco J, Garikano X, Garmendia Mujika M. Influence of geometric parameters of the flow fields on the performance of a PEM fuel cell. A review. Int J Hydrogen Energy 2012;37:15256–87.

[28] Zhong D, Lin R, Liu D, Cai X. Structure optimization of anode parallel fl ow fi eld for local starvation of proton exchange membrane fuel cell. J Power Sources 2018;403:1–10.

[29] Li Y, Pei P, Wu Z, Ren P, Jia X, Chen D, et al. Approaches to avoid flooding in association with pressure drop in proton exchange membrane fuel cells. Appl Energy 2018;224:42–51.

[30] Wang Y, Wang S, Wang G, Yue L. Numerical study of a new cathode flow-field design with a sub-channel for a parallel flow-field polymer electrolyte membrane fuel cell. Int J Hydrogen Energy 2018;43:2359–68.

[31] Liu H, Yang W, Tan J, An Y, Cheng L. Numerical analysis of parallel flow fields improved by micro-distributor in proton exchange membrane fuel cells. Energy Convers Manag 2018;176:99–109.

[32] Lin R, Ren YS, Lin XW, Jiang ZH, Yang Z, Chang YT. Investigation of the internal behavior in segmented PEMFCs of different flow fields during cold start process. Energy 2017;123:367–77.

[33] Santamaria AD, Bachman J, Park JW. Cold-start of parallel and interdigitated flow-field polymer electrolyte membrane fuel cell. Electrochim Acta 2013;107:327–38.
[34] Yuan P. Effect of inlet flow maldistribution in the stacking direction on the performance of a solid oxide fuel cell stack. J Power Sources 2008;185:381–91.
[35] Yuan P, Liu S. Effect of non-uniform inlet flow rate on the heat-up process of a solid oxide fuel cell unit with cross-flow configuration. Int J Hydrogen Energy 2016;41:12377–86.
[36] Wei L, Liao Z, Suo Z, Chen X, Jiang F. Numerical study of cold start performance of proton exchange membrane fuel cell with coolant circulation. Int J Hydrogen Energy 2019;44:22160–72.
[37] Wang F. -20 °C cold start of fuel cell engine. Shanghai Auto 2017;3–6.
[38] Jiang F, Fang W, Wang C. Non-isothermal cold start of polymer electrolyte fuel cells. Electrochim Acta 2007;53:610–21.
[39] Wang C. Fundamental models for fuel cell engineering. Chem Rev 2004;104:4727–66.
[40] Meng H. Numerical analyses of non-isothermal self-start behaviors of PEM fuel cells from subfreezing startup temperatures. Int J Hydrogen Energy 2008;33:5738–47.
[41] Huo S, Jiao K, Wan J. On the water transport behavior and phase transition mechanisms in cold start operation of PEM fuel cell. Appl Energy 2019;233–234:776–88.
[42] Thompson EL, Capehart TW, Fuller TJ, Jorne J. Investigation of low-temperature proton transport in nafion using direct current conductivity and differential scanning calorimetry. J Electrochem Soc 2006;153:A2351–63.
[43] Zhu Y, Lin R, Jiang Z, Zhong D, Wang B, Shangguan W, et al. Investigation on cold start of polymer electrolyte membrane fuel cells with different cathode serpentine flow fields. Int J Hydrogen Energy 2019;44:7505–17.
[44] Kulikovsky AA. Polarization curve of a PEM fuel cell with poor oxygen or proton transport in the cathode catalyst layer. Electrochem Commun 2011;13:1395–9.
[45] Weng F, Su A, Hsu C. The study of the effect of gas stoichiometric flow rate on the channel flooding and performance in a transparent. Fuel Cell 2007;32:666–76.
[46] Liu D, Lin R, Feng B, Yang Z. Investigation of the effect of cathode stoichiometry of proton exchange membrane fuel cell using localized electrochemical impedance spectroscopy based on print circuit board. Int J Hydrogen Energy 2019;1–10.
[47] Qu S, Li X, Hou M, Shao Z, Yi B. The effect of air stoichiometry change on the dynamic behavior of a proton exchange membrane fuel cell. J Power Sources 2008;185:302–10.
[48] Kulikovsky AA. The effect of stoichiometric ratio λ on the performance of a polymer electrolyte fuel cell. Electrochim Acta 2004;49:617–25.
[49] Qu S, Li X, Hou M, Shao Z, Yi B. The effect of air stoichiometry change on the dynamic behavior of a proton exchange membrane. Fuel Cell 2008;185:302–10.
[50] Iranzo A, Boillat P, Biesdorf J, Salva A. Investigation of the liquid water distributions in a 50 cm^2 PEM fuel cell : Effects of reactants relative humidity, current density, and cathode stoichiometry. Energy 2015;82:914–21.